Eastward-Propagating Intraseasonal Oscillation Represented by Chikira–Sugiyama Cumulus Parameterization. Part I: Comparison with Observation and Reanalysis

MINORU CHIKIRA

Research Institute for Global Change, JAMSTEC, Yokohama, Japan

MASAHIRO SUGIYAMA

Central Research Institute of Electric Power Industry, Tokyo, Japan

(Manuscript received 1 February 2013, in final form 15 August 2013)

ABSTRACT

The eastward-propagating intraseasonal oscillation represented by the Chikira–Sugiyama cumulus parameterization in an atmospheric general circulation model is compared with observations and reanalyses. The scheme is characterized by state-dependent entrainment rates that vertically vary affected by the environment. The zonal wavenumber–frequency power spectrum shows a strong signal corresponding to the Madden–Julian oscillation. The eastward-propagating feature of the convective region and accompanying anomalous zonal wind structure is well extracted by the first and second modes of the combined empirical orthogonal function (CEOF) with a reasonable explained variance for the first mode, though the second mode is not sufficiently reproduced. The basic features of the composited anomalous fields including moisture, temperature, and vertical and zonal winds resemble those of the reanalysis in both the free troposphere and surface air. The anomalous free-tropospheric moisture exhibits its westward tilt and the peak moist static energy of the surface air is shifted eastward as in the reanalysis. The anomalous low-level zonal wind changes its direction to the east of the convective center. The model's outstanding deficiencies include the weak convective activity over the Indian Ocean, weaker westward tilt, and seemingly underestimated shallow convection.

1. Introduction

The Madden–Julian oscillation (MJO) is the dominant variability in the tropical atmosphere on time scales shorter than a season (e.g., Madden and Julian 2005). It is a planetary-scale eastward-propagating mode, manifesting itself in various meteorological fields and oceans in the tropics. Its appearance may be characterized as a first-baroclinic Gill (1980) response forced by anomalous convection. Because of its scale, it affects many tropical meteorological phenomena, including active and break phases of the Indian and Australian monsoon (Yasunari 1979; Krishnamurti and Subrahmanyam 1982; Goswami 2005; Wheeler and McBride 2005), tropical cyclone activity (Liebmann et al. 1994; Maloney and Hartmann 2000), and triggering and termination of El Niño–Southern Oscillation (ENSO) events [e.g., Takayabu et al. (1999), Bergman et al. (2001), and Lau (2005) for more recent updates]. In addition to its tropical influences, the MJO affects midlatitude circulations (Ferranti et al. 1990); its near-global impact even on rainfall has been statistically demonstrated (Donald et al. 2006).

Despite of its importance and active research, the climate community is still struggling with the MJO (Slingo et al. 1996; Waliser et al. 2003; Sperber and Annamalai 2008). Although we can see some progress of the models' capabilities in general, Most of the Intergovernmental Panel on Climate Change (IPCC)-class general circulation models (GCMs) still suffer from poor simulations of the MJO (Lin et al. 2006). Recently, the U.S. Climate Variability and Predictability (CLIVAR) MJO Working Group (2009) proposed standardized diagnostic metrics, ranging from simple variance and correlation analyses to the multivariate empirical orthogonal functions and space–time spectra. Kim et al. (2009) applied those

Corresponding author address: Minoru Chikira, Research Institute for Global Change, JAMSTEC, 3173-25 Showa-machi Kanazawa-ku, Yokohama, Kanagawa 236-0001, Japan.
E-mail: chikira@jamstec.go.jp

DOI: 10.1175/JAS-D-13-034.1

techniques to the eight GCMs. Though some models compare reasonably with the observations, there remain many deficiencies, including a shorter MJO decay time scale in the models.

Even so, past studies have provided insight into the types of atmospheric model changes that lead to improved MJO simulations. These include 1) employing inhibition mechanisms associated with cumulus convection, 2) coupling to ocean models (Waliser et al. 1999; Hendon 2000; Kemball-Cook et al. 2002; Inness and Slingo 2003; Fu and Wang 2004; Sperber et al. 2005; Marshall et al. 2008), 3) improving the quality of the mean-state MJO (e.g., Inness et al. 2003; Sperber et al. 2005), and 4) increasing vertical resolution (Inness et al. 2001; Jia et al. 2008).

With regard to the first type, a school of the inhibition method is the requirement of the destabilization by large-scale forcing being larger than a certain threshold (e.g., Zhang and Mu 2005; Deng and Wu 2010). The method was devised through the analyses of intensive observations of moist convection, though its underlying physics is not fully understood.

Another school of the inhibition method is associated with the relation between free-tropospheric humidity and moist convection. New observational and modeling studies have shown that the free-tropospheric humidity has a significant control over moist convection (Numaguti et al. 1995; Brown and Zhang 1997; Sherwood 1999; Sherwood and Wahrlich 1999; Sobel et al. 2004; Biasutti et al. 2006). On the theoretical front, a series of papers (Raymond 2001; Fuchs and Raymond 2002, 2005; Raymond and Fuchs 2009; Sobel and Maloney 2012, 2013) explored a hypothesis that the MJO can be explained as a moisture mode. The moisture mode is a mode that originates from interaction between free-tropospheric moisture and convective activity under the weak temperature gradient (WTG) balance (Sobel et al. 2001), and whose behavior can be explained primarily by a humidity variable (Sugiyama 2009; Sobel and Maloney 2012, 2013).

Many GCMs have weak sensitivity of deep convection to free-tropospheric humidity (Derbyshire et al. 2004), but one can enhance the sensitivity by imposing a minimum entrainment rate (Tokioka et al. 1988; Lee et al. 2001, 2003; Lin et al. 2008), instituting a relative humidity threshold for deep convection (Wang and Schlesinger 1999; Maloney and Hartmann 2001; Maloney 2002; Zhang and Mu 2005; Suzuki et al. 2006; Lin et al. 2008) or altering a parameter related with reevaporation of falling precipitation (Maloney and Hartmann 2001; Grabowski and Moncrieff 2004; Maloney 2009; Kim et al. 2012). Some of these studies demonstrated improved simulations of the intraseasonal variability while others do not.

Recently, further progress in this direction was made by modifying the formulation of entrainment rate (Bechtold et al. 2008; Chikira and Sugiyama 2010; Del Genio et al. 2012; Kim et al. 2012). Bechtold et al. (2008) formulated the rate so that it varies vertically depending on environmental humidity in order to enhance the model's sensitivity to free-tropospheric humidity. They successfully represented a reasonable signal of the MJO in the power spectrum of outgoing longwave radiation (OLR) in their GCM.

While the formulation in Bechtold et al. (2008) was an ad hoc one, Chikira and Sugiyama (2010) sought a possibility of a more physically based scheme and adopted two already-existing formulations that had been proposed by Gregory (2001) and Neggers et al. (2002), together with the device of a new spectral representation of cloud types as in the Arakawa–Schubert scheme (Arakawa and Schubert 1974) suitable for the formulations. Both of the formulations were based on certain physical considerations and naturally had an enhanced sensitivity to free-tropospheric humidity without imposing any triggering schemes. Especially, Gregory's formulation exhibited a strong MJO signal in the OLR power spectrum. Del Genio and Wu (2010) compared the formulations of Gregory (2001), Neggers et al. (2002), and Bechtold et al. (2008) with the entrainment rate of the continental deep convection represented by their cloud-resolving model and demonstrated that the concept of Gregory's formulation reasonably works, though the others do not. Gregory's work largely relies on that by Grant and Brown (1999), which explored a similarity hypothesis for shallow cumulus. The Goddard Institute for Space Studies (GISS) GCM first used Gregory's formulation to investigate the change in updraft velocity in a warmer climate (Del Genio et al. 2007) and afterward provided better MJO-like waves with the optimized tuning parameters for waves (Del Genio et al. 2012; Kim et al. 2012).

We use the term Chikira–Sugiyama (CS) scheme for the one proposed by Chikira and Sugiyama (2010) with Gregory's entrainment rate. In a sense, it can be viewed as a modification of the Arakawa–Schubert scheme. However, many of its essential features described in their original paper (Arakawa and Schubert 1974) are replaced by different formulations that appeared afterward—for example, the cloud-base mass flux closure by Xu (1993) and Pan and Randall (1998), entrainment rate by Gregory (2001), and spectral representation by Chikira and Sugiyama (2010).[1]

[1] The CS scheme is the complex of the components proposed by many different researchers. We sincerely acknowledge these people and our intent on the use of this term is just for its reference.

While the relative humidity threshold method tends to produce only two modes, deep and shallow convection (the term ''shallow convection'' is used to represent convection whose top is around 800 hPa) depending on whether free-tropospheric relative humidity is higher or lower than the threshold, the CS scheme exhibits a smooth variation of cloud top along with free-tropospheric humidity. When the humidity has moderate values, the scheme tends to produce congestus clouds that detrain around 600 hPa.

The CS scheme improved the model's climatology as well as its variability in both of the atmospheric and coupled GCM for a wide variety of phenomena. The improvements include the resolution of the double intertropical convergence zone (ITCZ) problem and a better representation of the South Pacific convergence zone (SPCZ) (Chikira 2010; Watanabe et al. 2010; Hirota et al. 2011), which had long been the subject of many climate model studies. When coupled with an oceanic model, the model obtained a better amplitude of ENSO and some sensitivity experiments revealed that a parameter used in Gregory's formulation was a dominant controlling factor in the amplitude (Watanabe et al. 2011). Monsoon and its linkage with ENSO was also improved (Kim et al. 2011) and the life cycle of the boreal summer intraseasonal variation was the best represented among the Coupled Model Intercomparison Project, version 5 (CMIP5), models (Sperber et al. 2013).

Despite the rise of the superparameterization (Grabowski 2001; Khairoutdinov and Randall 2001) and the global cloud system–resolving model (CSRM) (Tomita et al. 2005; Miura et al. 2007), conventional GCMs still continue to be our primary tool for investigations, particularly for long-range predictions and projections of the climate. Moreover, understanding of complicated phenomena is achieved by their simplifications and the conventional GCMs with a cumulus parameterization have their unique role in bridging the gap between the global cloud-resolving models and simplified models—for example, the quasi-equilibrium tropical circulation model (Neelin and Zeng 2000).

This paper (Part I) compares the MJO-like waves produced by the CS scheme in an atmospheric GCM (AGCM) with observations and reanalyses in order to reveal to what extent the simulated MJO-like waves capture the various features of the MJO and identify the future subjects to be improved. The companion paper (Chikira 2013, hereafter Part II) further provides the detailed analyses of the free-tropospheric moisture variation accompanying the simulated MJO-like waves in order to obtain physical insights into controlling factors of MJO. Part I is also intended to provide background knowledge for understanding the analyses in Part II. The reasons for the use of the AGCM are 1) to make the understanding easier by removing the effect of the oceanic model particularly in Part II and that 2) the tuning parameters in the CS scheme in the coupled model was optimized for the amplitude of ENSO, which lead to a weaker signal of the MJO in the OLR spectrum than that in the AGCM.

An experimental design is described in section 2. The results with the tools provided by the United States' CLIVAR MJO Working Group (CLIVAR Madden–Julian Oscillation Working Group 2009) are provided in section 3 to show the model's performance in terms of the standardized metrics. The composited results of a wider variety of variables are provided in section 4. Finally, a summary and discussion are made in section 5.

2. Experimental design

Data analyzed in this work are identical with the AGCM experiments in Chikira and Sugiyama (2010). The AGCM is the atmospheric part of the Model for Interdisciplinary Research on Climate, version 4.1 (MIROC4.1). The model is a developing version and almost the same as MIROC5 (Watanabe et al. 2010) and characterized by three-dimensional primitive equations in a hybrid sigma–pressure (σ–p) coordinate with spectrum and semi-Lagrangian hybrid discretizations, a probability distribution function (PDF)-based prognostic cloud scheme, a two-stream k-distribution scheme for radiation with 111 channels, level 2.5 of the Mellor–Yamada turbulence scheme, an orographic gravity wave drag, the land surface model Minimal Advanced Treatments of Surface Interaction and Runoff (MATSIRO), and prognostic aerosols with direct and indirect effects.

As cumulus parameterization, the CS scheme is used with Gregory's entrainment formulation (Gregory 2001), which determines lateral entrainment rate as

$$\epsilon = C\frac{aB}{w^2},$$

where C and a denote tuning parameters from 0 to 1, and B and w denote buoyancy and vertical velocity of a cloud air parcel, respectively. The vertical velocity is calculated based on a simplified momentum equation in the vertical direction. For negative values of the buoyancy, the rate is set to be zero. Since the rate depends on the vertical velocity, the cloud-top height varies depending on cloud-base vertical velocity. Assuming that the cloud-base vertical velocity is distributed in a certain fixed range, cloud types with the different cloud-top height are spectrally represented. Although it is common for other

GCMs to adopt a shallow convection scheme separately from a deep one, this scheme represents both deep and shallow convection continuously in this unified framework as in the Arakawa–Schubert scheme. If buoyancy is smaller, the vertical velocity is less accelerated and the rate naturally becomes larger, resulting in the occurrence of shallow convection.

The horizontal resolution is T42 with 56 levels. A relatively higher vertical resolution is adopted considering importance of the vertical variation in entrainment rate. Climatology of observation is used for the sea surface temperatures (SSTs) and sea ice distribution. The integration is continued for 15 years and the last 10 years are analyzed.

3. Results with tools of U.S. CLIVAR MJO Working Group

Analyses of this and the next sections are based on the daily mean outputs of the experiments, observation, and reanalysis. With regard to the reanalysis, the daily mean is created from 6-hourly products. The monthly mean data are also used. This section adopts methods and tools proposed by the U.S. CLIVAR MJO Working Group (CLIVAR Madden–Julian Oscillation Working Group 2009), which aimed to provide standardized metrics on the MJO, and was used to examine eight AGCMs in Kim et al. (2009).

a. Wheeler–Kiladis diagram

Figure 1 shows the zonal wavenumber–frequency power spectra of the symmetric component of the OLR and zonal wind at 200 hPa divided by the background power (the so-called Wheeler–Kiladis diagram), which was preprocessed according to a series of procedures described in Wheeler and Kiladis (1999) using the model result, Advanced Very High Resolution Radiometer (AVHRR; from 1979 to 2005; Liebmann and Smith 1996) and National Centers for Environmental Prediction (NCEP) reanalysis (from 1979 to 2005; Kalnay et al. 1996) between 15°S and 15°N, including all the seasons. The background power means a power spectrum smoothed in both wavenumber and frequency. The intent of the division by the background power is to show only signals that are statistically significant against the background noise. See Fig. 10c in Chikira and Sugiyama (2010) for the antisymmetric component.

The model produces a strong signal of $n = 1$ equatorial Rossby (ER) waves [n denotes a meridional mode number as in Matsuno (1966)], though it is overestimated and excessively spreads to longer periods in the OLR. Although the equivalent depth of Kelvin waves tend to be overestimated in most GCMs (Lin et al. 2006), our model seems to provide a reasonable depth, though the signals tend to be underestimated. The model shows unrealistically strong signals where the zonal wavenumber is negative and the period is less than 10 days—the area of "tropical depression" disturbances described in, for example, Takayabu and Nitta (1993) and Dunkerton and Baldwin (1995). Although the reason is not clear, the same figure for our coupled model shows much better signals for this area (Watanabe et al. 2010). The signal of the MJO is comparable to the observation, though it tends to spread to longer periods and larger wavenumber; that is, the simulated MJO-like waves tend to be rather stationary and smaller in longitude than the observation. The zonal wind is better represented in the model than the OLR.

b. Climatology and variance

Figures 2a–f show the annual mean, unfiltered variance and 20–100-day filtered variance of OLR in the AVHRR and model. The variance is against the climatological daily mean and the bandpass filtering is based on a 201-point Lanczos filter.

The annual-mean OLR in the model is overestimated over the Indian Ocean and underestimated over the Bay of Bengal and the western coast of Central America. The bias is consistent with that of the annual-mean precipitation in these regions (Chikira 2010). The same bias is seen in many atmospheric GCMs (Kim et al. 2009). In our case, the problem is improved if coupled with oceanic models (Watanabe et al. 2010). Reflecting the mean bias, the unfiltered variance is underestimated in the Indian Ocean and overestimated in the western coast of Central America. Besides, it tends to have larger values over the whole globe and especially around the Maritime Continent. The 20–100-day filtered variance shows a similar pattern to the unfiltered counterpart. While the observation shows the largest peak in the Indian Ocean, the model does in the western Pacific. Again, the signal tends to be overestimated over the whole globe. A similar deficiency is seen in many AGCMs (Kim et al. 2009).

The Wheeler–Kiladis diagram for the OLR in the model (Fig. 1b) shows the overestimated westward-propagating signals in the period between 30 and 80 days, which is one of the reasons for the model biases seen in Figs. 2d and 2f. To remove the bias coming from the westward-propagating waves, the variance is taken for the 20–100-day filtered OLR where the westward-propagating Fourier components were removed (Figs. 2g,h). In Fig. 2h, the global distribution of the variance better agrees with that in the observation. The largest variance is still seen in the western Pacific, which shows that the MJO-like waves are predominant there. The signal tends to be overestimated over the whole globe. In section 4, it is shown that one of the reasons is the

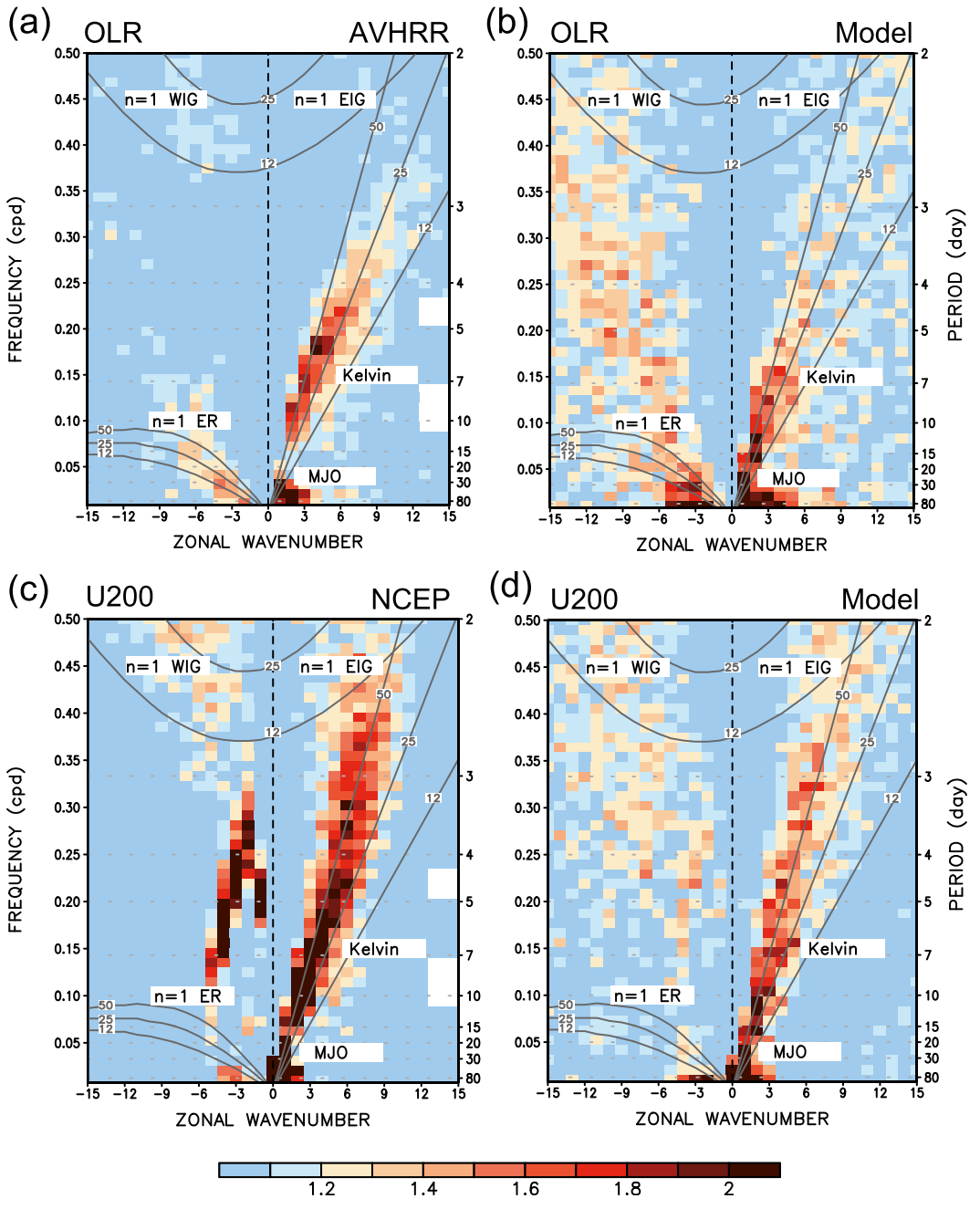

FIG. 1. Zonal wavenumber–frequency power spectra of the symmetric component of (a),(b) OLR and (c),(d) zonal wind at 200 hPa divided by the background power according to Wheeler and Kiladis (1999): (b),(d) model results, (a) AVHRR, and (c) NCEP reanalysis. Dispersion curves of the odd-meridional-mode-numbered equatorial waves for the three equivalent depths of 12, 25, and 50 m are indicated by red lines. See text for the abbreviated terminology of the waves. The unit of frequency and period are cycles per day (cpd) and days, respectively.

overestimated amplitude of the cloud water accompanying the MJO-like waves.

c. *Combined EOF*

Following Wheeler and Hendon (2004) and Kim et al. (2009), the first and second mode of the combined empirical orthogonal functions (CEOFs) for the OLR, zonal wind velocity at 850 (U850) and 200 hPa (U200) were extracted using 10-yr outputs of the model and a set of the AVHRR (for OLR) and NCEP reanalysis (from 1979 to 2005). The results are shown in Fig. 3. The set of the AVHRR and NCEP reanalysis are referred to

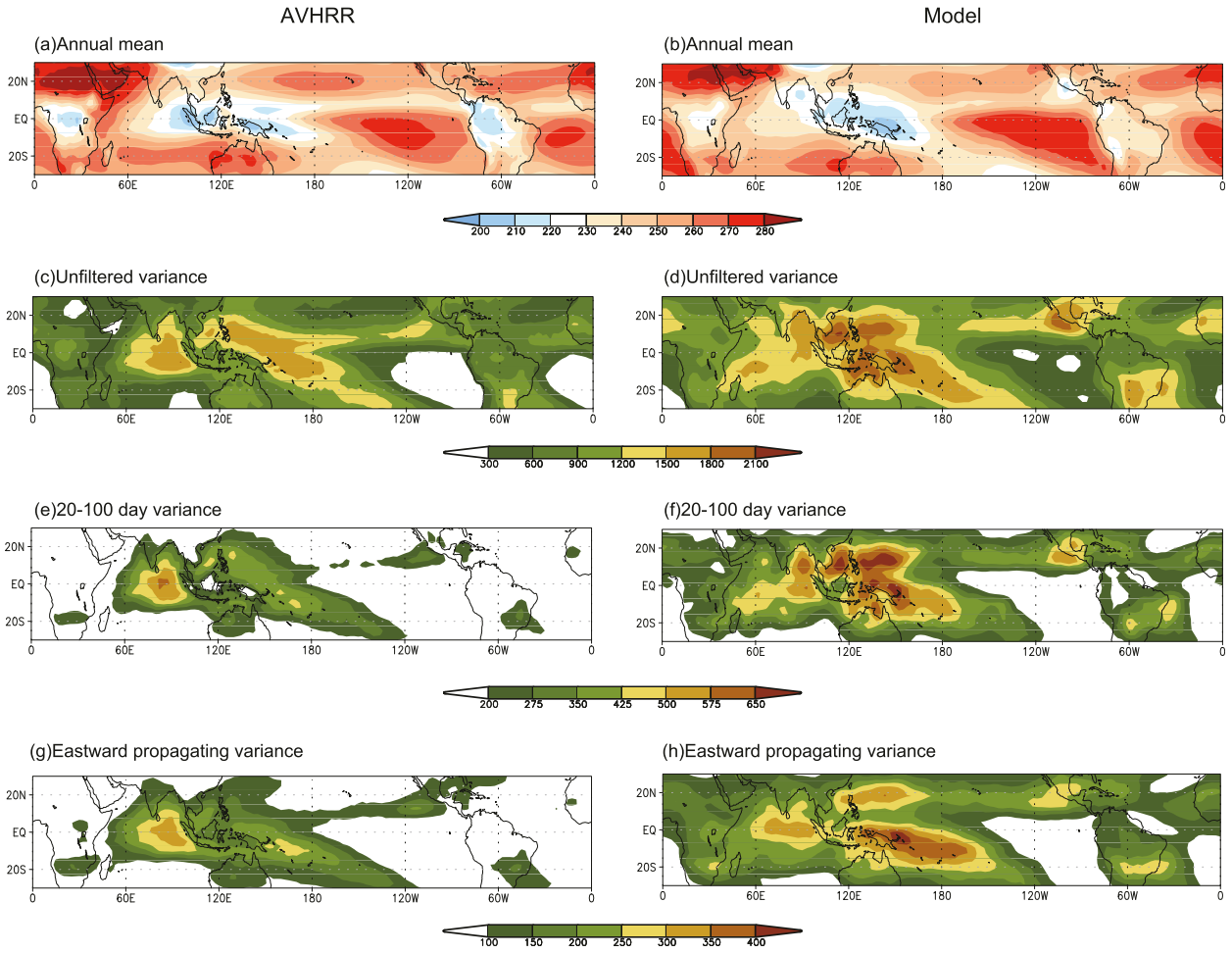

FIG. 2. (a),(b) Annual-mean OLR ($W\,m^{-2}$), (c),(d) variance of the OLR ($W^2\,m^{-4}$), and (e),(f) variance of the 20–100-day bandpass-filtered OLR ($W^2\,m^{-4}$) in the (left) AVHRR and (right) model. (g),(h) As in (e),(f), respectively, except the westward-propagating components are removed. Note that scales are different in the bottom three rows.

by a term ''observation'' for simplicity. In advance of the computing, the anomalies for all three variables were taken against the climatological daily mean. Next, the products were 20–100-day filtered and averaged between 15°S and 15°N. Then, the amplitudes of the three variables were normalized by square roots of the zonal mean temporal variances, respectively.

The first mode in the model reasonably represents the general structure of the mode in the observation. U850 is easterly over the Western Hemisphere and changes its sign to the east of the convective peak. U200 has an opposite sign to U850 and also changes its sign at the same longitude. The width of the negative OLR region is narrower than that in the observation, which is consistent with the overestimated zonal wavenumber for the MJO-like waves seen in Fig. 1b. Besides, its position is displaced eastward, reflecting the lack of the convection in the Indian Ocean (Fig. 2). U200 shows a positive bias over the entire longitude, though its amplitude seems plausible. As for the second mode, the model performance is not sufficient in representing a maximum around 80°E and a minimum around 150°E for the OLR, though a similar pattern exists that is obscured and displaced eastward. Similar deficiencies are also seen in many AGCMs (Kim et al. 2009). U850 and U200 are well represented except for its eastward shifts. The same analysis was made for the same dataset where the westward-propagating Fourier components were removed. But the result was not qualitatively improved for both the first and second modes (not shown), which shows that the deficiency in the second mode is not coming from the overestimated westward-propagating intraseasonal signals but is inherent in the model MJO-like waves.

Figure 4 shows the explained variance for each of the CEOF modes. In the observation, the first two modes

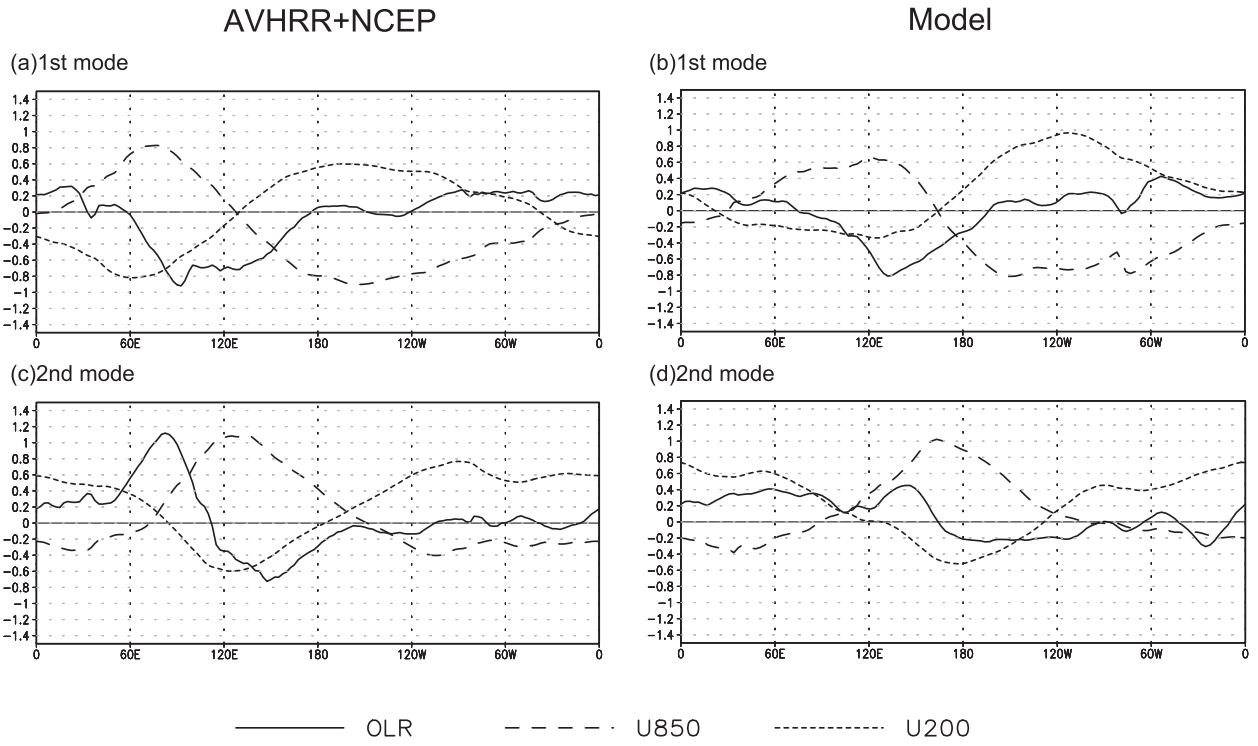

FIG. 3. (a),(b) First mode of combined EOFs for OLR (solid) and zonal wind velocity at 850 (long dashed) and 200 hPa (short dashed) in the (left) observation and (right) model. (c),(d) As in (a),(b), but for second mode. Abscissa and ordinate are longitude and normalized amplitude, respectively. See text for details of the computing.

are distinct from the other higher modes and the percentages of the first and second modes have similar values of around 20%. In the model, the magnitude of the first mode is 19.96%, which is very close to the observation and this is the best result if compared to any eight models examined in Kim et al. (2009). Although the percentage of the second mode, 14.51%, is underestimated, the value is relatively reasonable among those eight models. Table 1 shows the explained variance for each of the variable for the CEOF. The zonal wind features are better represented than the convective counterpart as in other models (Kim et al. 2009).

To assess whether the extracted modes are physically meaningful and distinct from the corresponding red noise, the power spectrum density for the principal components of the first (PC1) and second (PC2) modes is shown in Fig. 5. The time series of the PC1 and PC2 were created by projecting the CEOFs onto unfiltered data where the seasonal cycles are removed. The abscissa is frequency in logarithmic scale and the ordinate is the power spectrum density multiplied by frequency. The area under the density lines in any frequency band is equivalent to the corresponding explained variance. The red lines indicate the 95% confidence limit for the corresponding red-noise spectra computed as the lag-1 autocorrelation. The power for the model's PC1 is sufficiently significant between 30- and 80-day periods, but that for the PC2 is largely underestimated. Its values are close to the 95% confidence level around an 80-day period, while it is sufficiently strong around 30 days. The peak values for the model's PC1 and PC2 is shifted toward shorter periods compared to the observation. The variance explained by 30–80-day band for the PC1 and

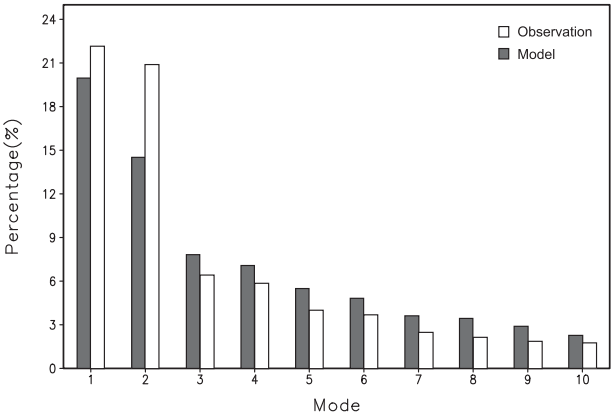

FIG. 4. Explained variance for each of the CEOF modes in the model (gray) and the observation (white).

TABLE 1. Explained variance for each variable of the CEOF.

	First mode			Second mode		
	OLR	U850	U200	OLR	U850	U200
Model	9.62	26.85	23.41	5.9	17.72	19.91
AVHRR+NCEP	13.21	31.73	21.66	15.91	23.11	23.78

PC2 is 42.19% and 32.80% for the model and 54.98% and 57.88% for the observation, respectively. Although the model's density for the PC1 has sufficiently large values between 30 and 80 days, it is also larger outside this range, resulting in the underestimation of the explained variance for the PC1.

The squared coherency and phase difference between the PC1 and PC2 (hereafter, these are the raw time series and are not the projection of the CEOFs onto unfiltered data) are shown in Fig. 6. The coherency of the model well agrees with the observation within a 30–80-day period. The mean coherencies within the range are 0.74 and 0.78 in the model and the observation, respectively. The model's value is the best one among the eight models examined in Kim et al. (2009). Although the model's second mode is not well represented, it is highly coherent with the first mode. The model's coherency tends to be high even outside 30–80 days, which appears to be explained by that the power spectrum of the MJO-like waves spreads toward both lower and higher frequency compared to the observation (Fig. 1b). The phase difference between the PC1 and PC2 shows that the first mode tends to lead the second one by ¼ cycle.

Figure 7 shows examples of the time development of the normalized PC1 and PC2 from 1 November to 30 April. The PC1 and PC2 are normalized by the respective standard deviation for the period. The starting year is 1979 for the observation and the second year of the 10-yr outputs for the model. Since the PC1 and PC2 are coherent and the PC1 leads the PC2 by ¼ cycle, the set of the PC1 and PC2 tends to move counterclockwise in the diagram of Fig. 7 in both the observation and model.

To obtain life-cycle composites of the MJO-like waves, eight phases were defined according to the normalized PC1 and PC2 as shown in Fig. 7. The magnitude of the wave was defined by $(\mathrm{NPC1}^2 + \mathrm{NPC2}^2)^{1/2}$, where NPC1 and NPC2 are the normalized PC1 and PC2, respectively. Then the composites for a given phase were made from the bandpass filtered anomalies of the OLR and wind velocity at 850 hPa of all days that corresponded to the phase when the magnitude was more than or equal to 1 between 1 November and 30 April. The products of the observation and model are shown in Figs. 8 and 9, respectively.

Figure 9 clearly shows that the two leading modes of the CEOFs in the model correspond to eastward-propagating waves, though the convective peak tends to lie over the Maritime Continent, unlike the observation. The enhancement of the easterly low-level wind to the east of the convective peak is well represented, though that of the westerly wind to the west of the peak tends to be underestimated.

4. Composited results

The aim of the previous subsection is to examine if the basic structure of the MJO is extracted as the principal modes of CEOFs. This section further compares the detailed composited structures for a wider variety of variables.

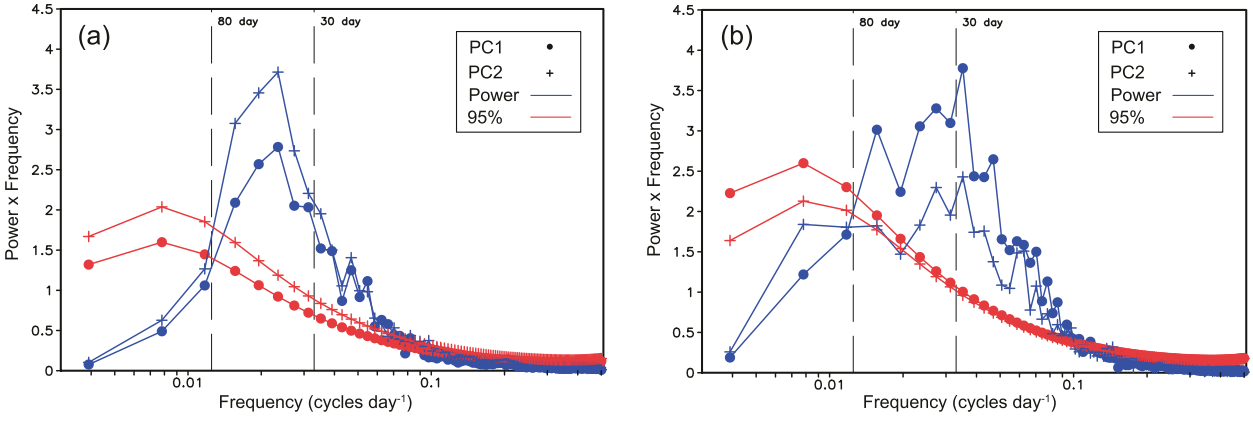

FIG. 5. Power spectra for the PC1 and PC2 multiplied by frequency (blue) in the (a) observation and (b) model. The red lines indicate the 95% confidence limit for the corresponding red-noise spectra. Abscissa is frequency in logarithmic scale. The 30- and 80-day periods are indicated by dashed lines.

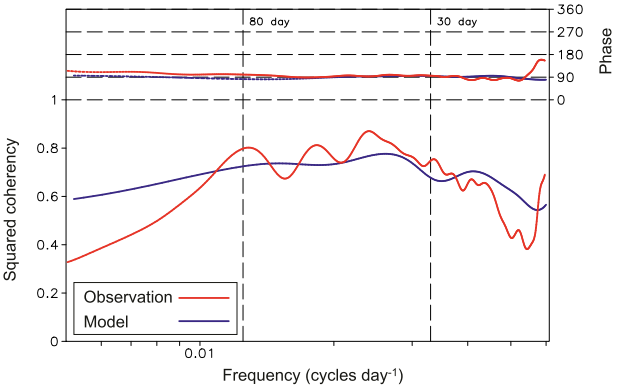

FIG. 6. (bottom) Squared coherency and (top) phase difference (°) between the PC1 and PC2 in the model (blue) and the observation (red).

a. Method

To select clear events corresponding to the MJO-like waves, the anomaly of the daily mean OLR was first taken against the climatological daily mean, which was smoothed out in advance by a 5-day running average to remove the fast variation. The compositing process is based on the local minima of the anomaly that was bandpass filtered 1–5 in zonal wavenumber and 20–100 days in period and then latitudinally averaged from 10°S to 10°N. Furthermore, only the events were chosen that satisfy the following conditions. The minimum must be between 60°E and 150°W. This range is determined considering that the model's MJO-like waves tend to be located more eastward than the observation as seen in Fig. 9. The minimum must propagate eastward at least 60° through which the minimum values must be less than -0.7σ, where σ is the standard deviation of the filtered anomaly. The mean unfiltered anomaly over $\pm 10°$ in longitude with respect to the minima during the propagation must be less than -1.2σ. Although the composites are taken for all the seasons including summer when clear MJO events are obscured in the observation, the events in summer tend to be naturally filtered out by applying all the above conditions. Many settings of the conditions were tested and the above specific setting was determined by manually examining if the selected events correspond to the clear MJO-like waves. However, the composited results do not depend on the details of the conditions in a qualitative sense.

The result is compared with the Interim European Centre for Medium-Range Weather Forecasts (ECMWF) Re-Analysis (ERA-Interim) dataset with the period from 1989 to 2005. The OLR provided by AVHRR with the same period is used when compositing the reanalysis. The daily mean variables are used for the composites. In the case of ERA-Interim, the daily mean is made by averaging the 6- or 3-hourly data.

b. Results

Figure 10 shows the number of composited events per year as a function of longitude. As one can expect from the results so far, the model underestimates the number of events over the Indian Ocean, but it is quite reasonable in other regions. Although the longitudinal range for the composites is extended up to 150°W, the events

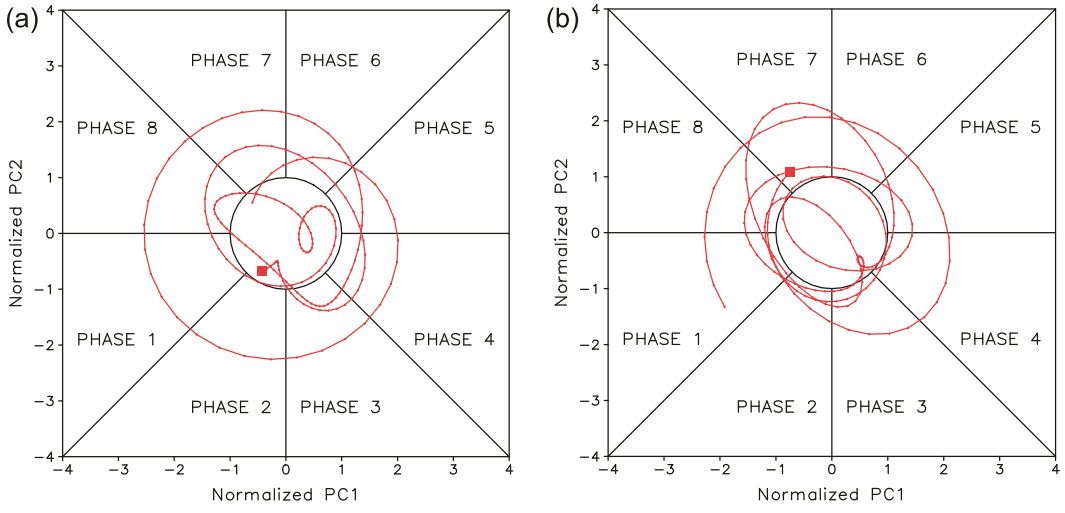

FIG. 7. Time development of the normalized PC1 and PC2 from 1 Nov to 30 Apr in the (a) observation and (b) model. The PC1 and PC2 are normalized by the respective standard deviation for the period. The values for the starting date are indicated by the red squares. The starting year is 1979 for the observation and the second year of the 10-yr outputs for the model. The definition of the phase used for the phase composites is shown. The radius of the circle located at the center is 1.

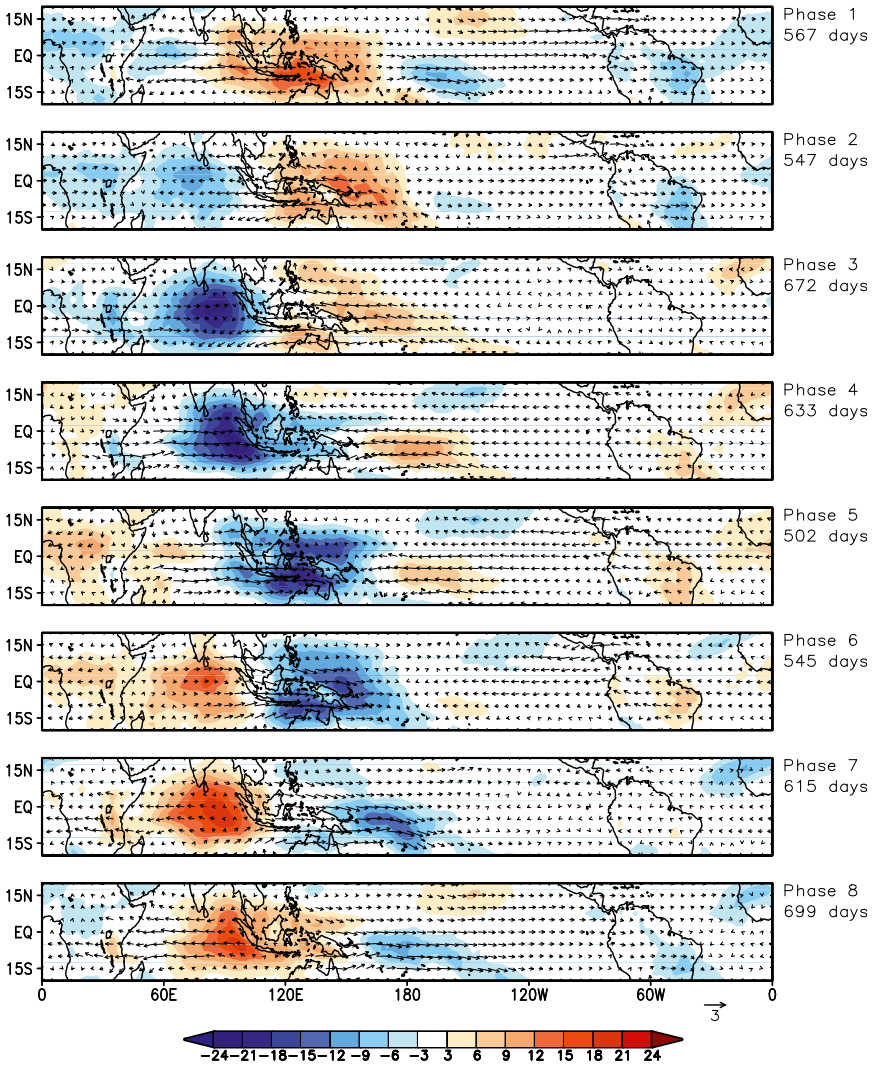

FIG. 8. Phase composites of the OLR (shading; $W m^{-2}$) and U850 (vectors; $m s^{-1}$) in the observation. The phase and the number of the days used for the composites are indicated on the right side. See text for the details of the procedure.

around the region is scarce and do not contribute to the composited fields significantly.

Figure 11 shows the latitudinally averaged specific humidity composited in different longitudinal ranges for the reanalysis and model. The selected variables are shown as departures from the time mean between −30 and 20 relative days. Considering that the peak moisture anomaly tends to be located to the south of the equator between 150°E and 150°W (not shown), the latitudinal range for the average is from 10°S to 10°N between 60° and 150°E but from 15°S to 5°N between 150°E and 150°W. Overall, the model produces less westward tilt, but it is significant between 120° and 150°E, as in the reanalysis. The peak moisture anomaly is seen at higher level, suggesting the lack of shallow convection. Reflecting the underestimation of the events over the Indian Ocean, the moisture anomaly is obscured between 60° and 90°E. In both the reanalysis and model, the tilt becomes weak between 180° and 150°W.

Hereafter, the composites are taken in the whole longitudinal range (60°E–150°W) and shown as departures from the time mean between −30 and 20 relative days. Figures 12a and 12b show the specific humidity anomaly at 600 hPa. Since the peak moisture anomaly tends to be located to the south of the equator between 150°E and 150°W in both the reanalysis and model, and the contribution of the events between this range is larger in the model (Fig. 10), the model shows a southward shift of the peak anomaly. Hereafter, the range of latitudinal average is from

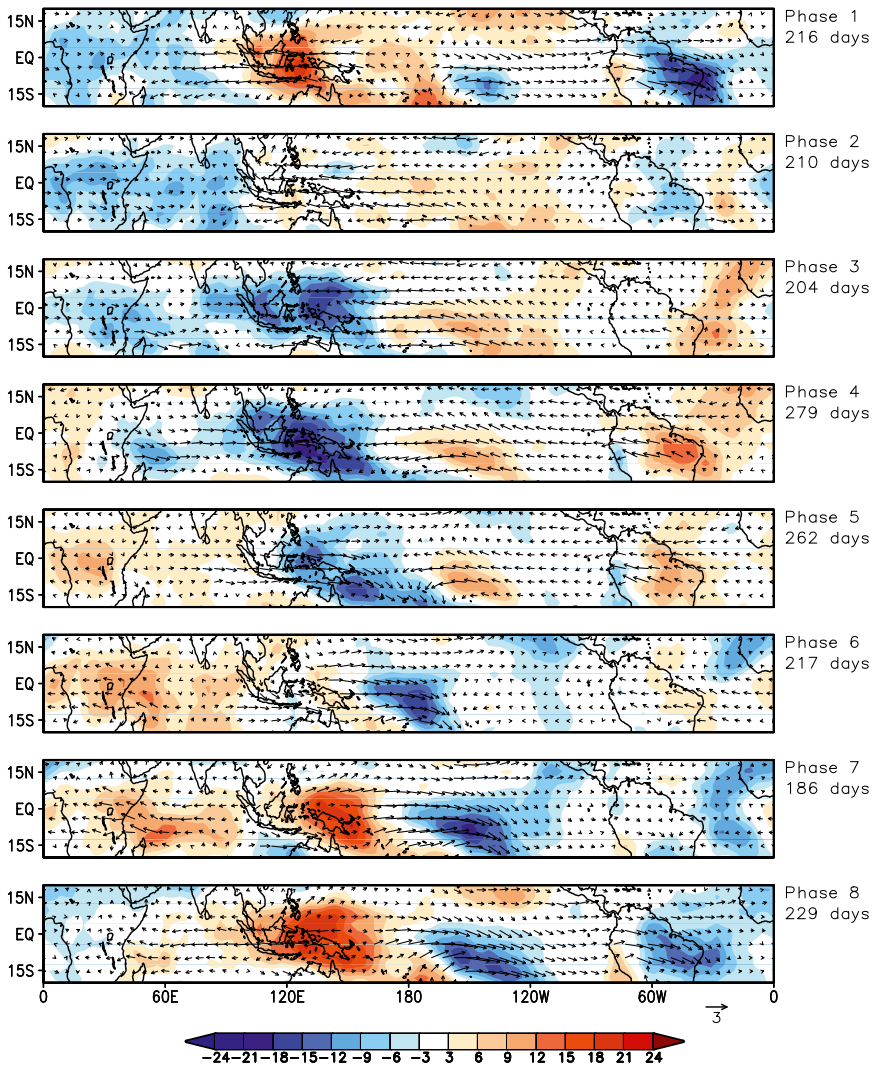

FIG. 9. As in Fig. 9, but for the model.

10°S to 10°N for the reanalysis and from 15°S to 5°N for the model.

The latitudinally averaged specific humidity, relative humidity, and cloud water anomaly are shown in Figs. 12c–h. Although the large relative humidity anomaly spreads in the whole upper troposphere, the positive cloud water anomaly has a sharp peak around 500 hPa in both the reanalysis and model, suggesting active cumulus detrainment around this level. In the model, the PDF-based large-scale cloud scheme (Watanabe et al. 2009) is considered to produce large skewness of the total water owing to the cumulus detrainment there. The model has a larger amplitude of the cloud water than that of the reanalysis.

The model shows an overestimated amplitude of the composited OLR (Fig. 13a) corresponding to the larger cloud water anomaly compared to the reanalysis, which also explains the overestimated OLR variance in Fig. 2h. As for the precipitation, the model is compared to the daily product of the Global Precipitation Climatology Project (GPCP) from 1997 to 2005 and 3-hourly forecast data of ERA-Interim. The model result is quite similar to the GPCP product, while the forecast data shows the eastward shift of its peak unseen in the others (Fig. 13b). The 2-m temperature anomaly shows its negative peak around the center of the convective area (Fig. 13c), corresponding to the enhanced downdraft activity there. The positive peak of the 2-m specific humidity anomaly is shifted eastward (Fig. 13d), which mostly explains the moist static energy anomaly distribution (Fig. 13e). Note that the units for the temperature and specific humidity are the same but their scales are not. The model produces qualitatively similar results to the reanalysis for both of the temperature and specific humidity, though

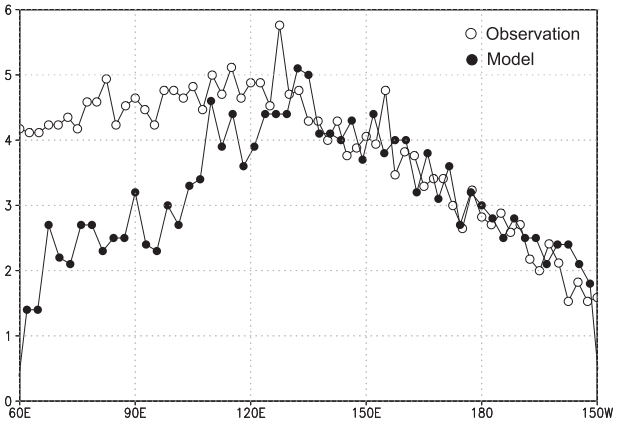

FIG. 10. Number of composited events per year as a function of longitude for the model (solid circle) and the AVHRR (open circle).

the eastward shift of the specific humidity and moist static energy is smaller. The eastward shift of the peak precipitation anomaly in the reanalysis seems to correspond to that of the moist static energy.

The 10-m zonal wind velocity anomaly shows a close resemblance between the model and reanalysis (Fig. 13f). However, the model's 10-m wind speed shows its maximum over the convective area while it shifts westward in the reanalysis (Fig. 13g). The reason is that the model overestimates the magnitude of the surface meridional wind velocity there (not shown). The surface latent heat flux in the reanalysis shows its westward shift reflecting that of the 10-m wind speed and the negative anomaly of the 2-m specific humidity to the west (Fig. 13h). The 10-m wind speed bias in the model causes the maximum surface latent heat flux nearer to the OLR minimum. In both the reanalysis and model, the peak surface sensible heat flux is located around 0 days despite the westward shift of the surface wind speed (Fig. 13i). It could be explained by the negative peak in the 2-m temperature around there, which leads to enhanced static instability near the surface. The amplitude of the model's surface sensible heat flux is smaller than that in the reanalysis presumably because of the smaller amplitude of the 2-m temperature. Note that the surface latent and sensible heat flux in the reanalysis means the 3-hourly forecast products of ERA-Interim with the initial condition of the reanalyzed fields.

The eastward shift of the 2-m specific humidity is not explained by the surface latent heat flux whose positive peak is shifted westward. Since the 2-m temperature anomaly does not show larger values to the east, the 2-m saturated specific humidity does not explain the shift either. Considering that the contribution of the horizontal advection terms to the boundary layer–mean total water is much smaller than those of the surface and boundary layer–top fluxes in the model (not shown), the eastward shift could be explained by the boundary layer–top flux. The larger total water to the east of the OLR minimum is considered to lead to less drying owing to the entrainment at the boundary layer top.

Figures 14a and 14b show the potential temperature anomaly. It has a large positive peak at 300 hPa over the convective area and more moderate one in the lower to middle troposphere around −10 relative days. The temperature-anomaly distribution is better understood by examining the saturation equivalent potential temperature, which shows the similar anomaly distribution. Since the peak surface-air moist static energy is shifted eastward, the free-tropospheric temperature over the eastern side of the convective center would increase through convective adjustment to the moist adiabatic temperature profile of the surface air (Betts 1986; Betts and Miller 1986) if there was no entrainment. However, the free troposphere there is drier than the convective center and the entrainment of the air should lead to a lower cumulus cloud top maintaining the higher temperature only in the lower troposphere, but not in the upper counterpart. On the other hand, the large positive free-tropospheric moisture anomaly over the convective center allows deep convection to reach higher and keep the higher temperature in the upper troposphere in spite of the smaller moist static energy of the surface air compared to the eastern side. The model lacks the negative temperature peak at 650 hPa seen in the reanalysis over 0–5 relative days. The reason may be the smaller amount of the rainfall evaporation. The lack of this negative temperature peak as well as the weak negative peak in the 2-m temperature over the convective area might lead to excessively lower sea surface pressure and cause the bias in the surface wind speed.

Figures 15a–d shows the apparent heat source (Q1) and apparent moisture sink (Q2) anomalies (Yanai et al. 1973). The model exhibits the top-heavy heating profile as seen in the reanalysis. With regard to Q2, the model's peak sink in the upper troposphere is similar to the reanalysis. However, the model has another peak around 800 hPa unseen in the reanalysis presumably because of the underestimation of shallow convection, which could be the major factor in the model's less positive moisture anomaly in the lower troposphere. The pressure velocity has its minimum in the upper troposphere, corresponding to the top-heavy heating profile (Figs. 15e and 15f). The anomalous zonal velocity shows the greater magnitude to the west of the OLR minimum than the east and its convergence area extends up to 400 hPa, corresponding to the top-heavy heating profile. In all the variables seen in Fig. 15, the model lacks the westward

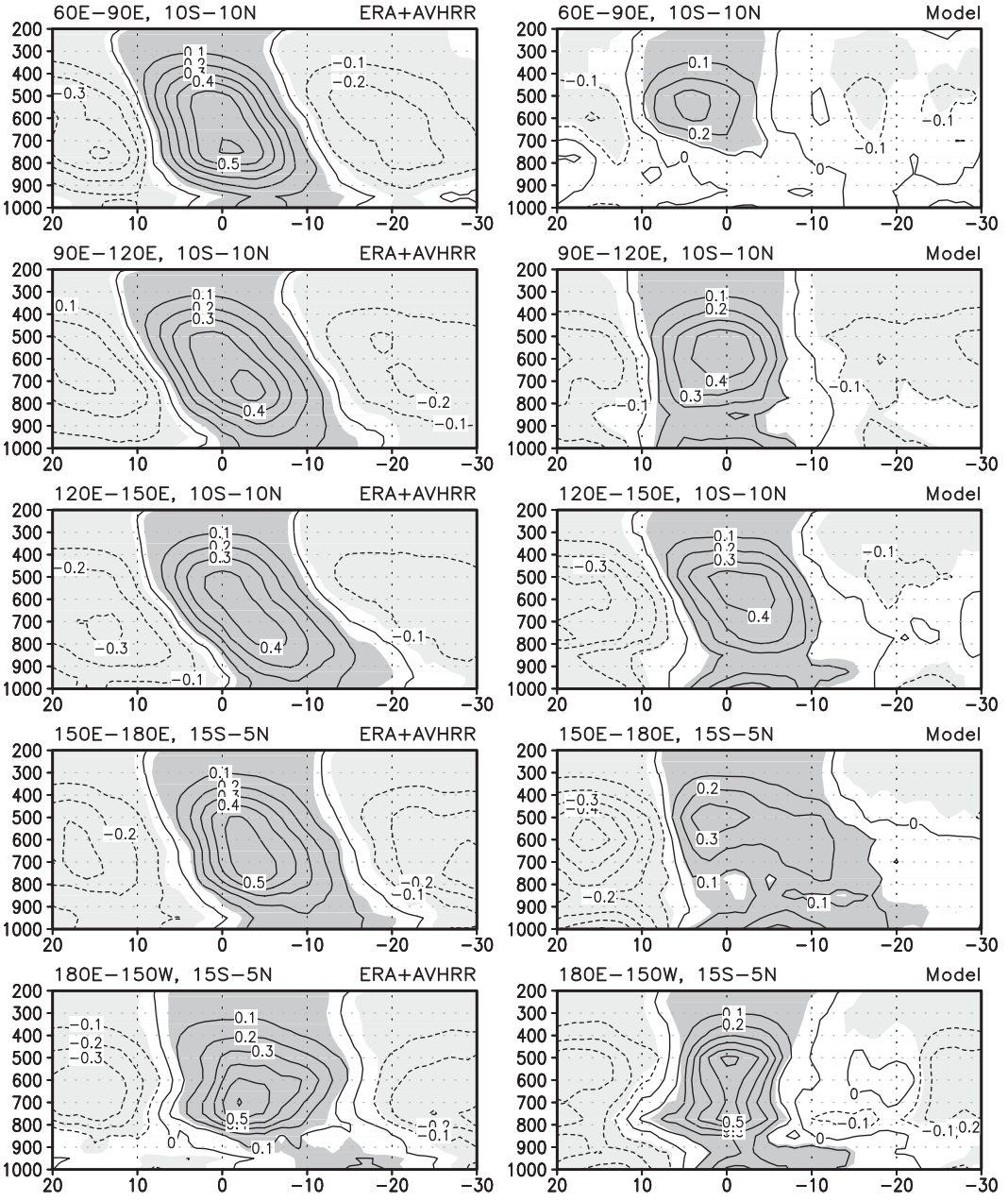

FIG. 11. Composited specific humidity ($g\,kg^{-1}$) in different longitudinal ranges for the (left) ERA-Interim and (right) model. The longitudinal and latitudinal range for the composites is indicated above each panel. Ordinate and abscissa are pressure (hPa) and relative time (days), respectively. The 95% significance level is indicated by gray.

tilt. The less eastward shift of the model's 2-m specific humidity may correspond to the less westward tilt of the free-tropospheric humidity.

5. Summary and discussion

The MJO-like waves produced by the Chikira–Sugiyama scheme in the AGCM was compared with the observation and reanalyses in order to reveal to what extent the simulated waves capture the various features of the MJO and identify the future subjects to be improved. First, several analyses were made using the tools developed by the U.S. CLIVAR MJO Working Group to show the model's performance in terms of the standardized metrics. Then, a wider variety of composited variables were further examined with our own method.

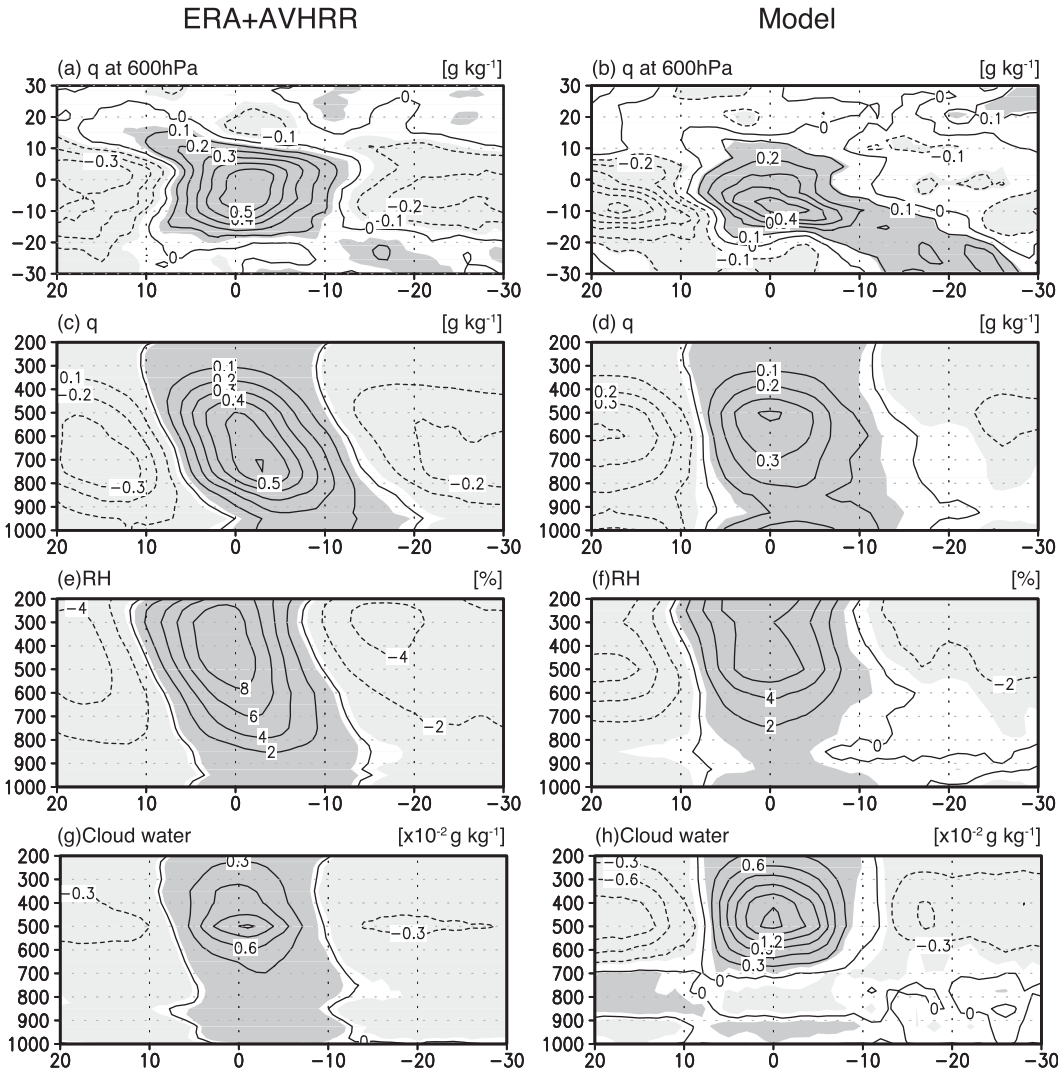

FIG. 12. (a),(b) Specific humidity at 600 hPa and latitudinally averaged (c),(d) specific humidity, (e),(f) relative humidity, and (g),(h) cloud water in the (left) ERA-Interim and (right) model. Abscissa is relative time (days). Ordinate is latitude in (a),(b) and pressure (hPa) in (c)–(h). Units are indicated above each panel.

The model showed a strong signal corresponding to the MJO in the Wheeler–Kiladis diagram, though the signal tends to spread to a longer period and a higher zonal wavenumber than the observation. The model underestimates the convective activity over the Indian Ocean and the excessively large OLR variance is seen over the western Pacific, as in many other AGCMs. One of the reasons for the overestimation is considered to be a too-large amplitude of the cloud water.

The model's first mode of the combined EOFs for the OLR and zonal winds at 850 and 200 hPa successfully captures the overall feature of the MJO seen in the observation and reanalysis. Its explained variance is very close to that of the observation and has the best value compared with the eight models examined in Kim et al. (2009). However, the OLR minimum is shifted eastward compared to the observation, reflecting the lack of convection over the Indian Ocean. The longitudinal width of the negative OLR anomaly is narrower. The model's performance is not enough to successfully represent the second mode, especially its OLR distribution. Despite the poor representation of the second mode, the model succeeds in representing the high coherency between the first and second modes and their phase difference. Defining the phase with the PC1 and PC2, the phase composites were taken for the OLR and wind velocity at 850 hPa. The results demonstrate that the model's first and second modes clearly correspond to the eastward propagation of the fields, though the

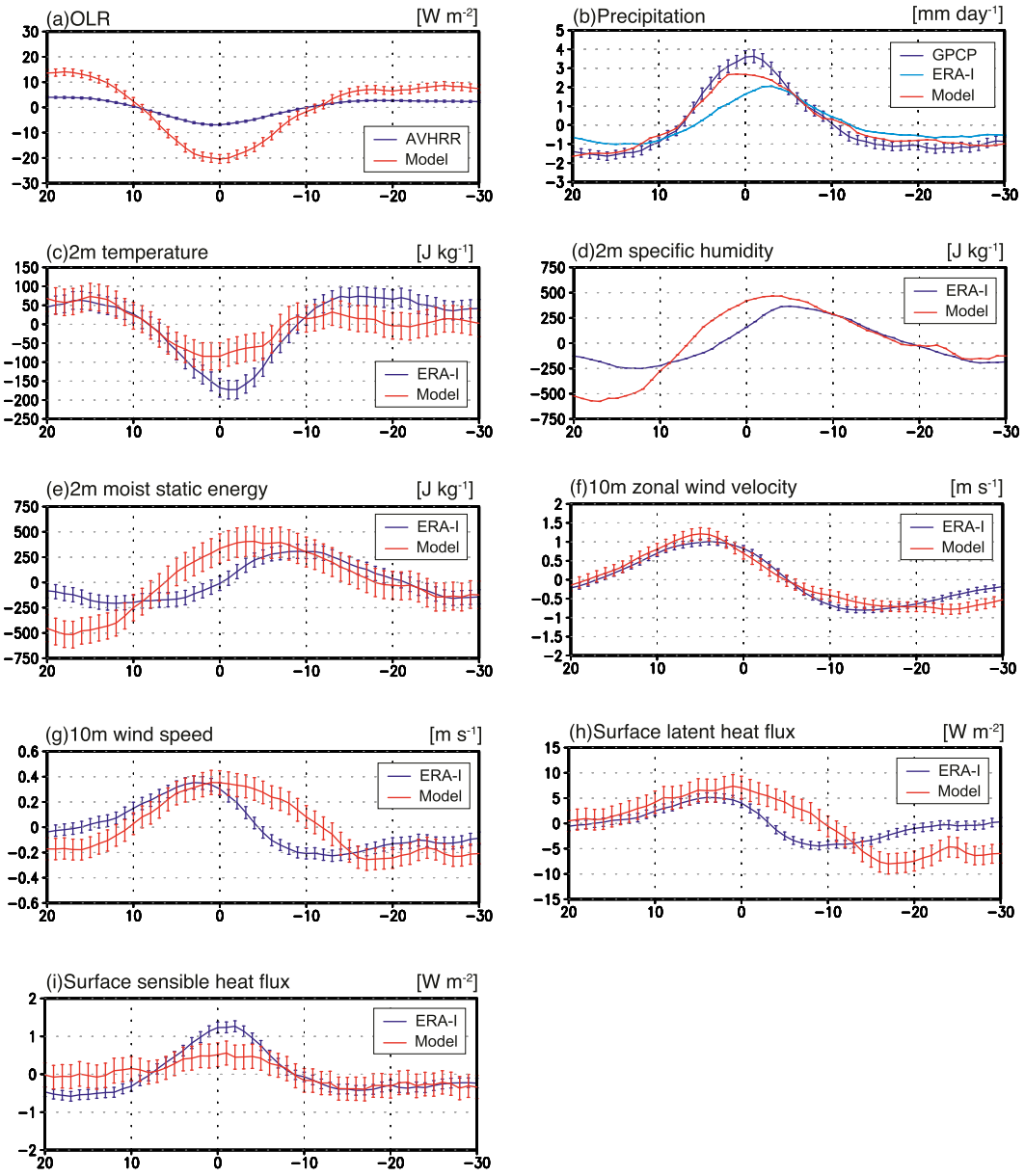

FIG. 13. Latitudinally averaged (a) OLR, (b) precipitation, (c) 2-m temperature, (d) 2-m specific humidity, (e) 2-m moist static energy, (f) 10-m zonal wind velocity, (g) 10-m wind speed, (h) surface latent heat flux, and (i) surface sensible heat flux, where red lines indicate the model. Blue lines in (a), (b), and (c)–(i) indicate the AVHRR, GPCP, and ERA-Interim, respectively. Sky blue in (b) indicates the ERA-Interim. The 95% confidence intervals are indicated by error bars. Lines without error bars mean that the confidence intervals are negligible compared to the amplitude of the variables. Units are shown above each panel.

convective region tends to stay over the Maritime Continent, unlike the observation.

The composites of a wider variety of variables were taken based on the local minima of the bandpass-filtered OLR anomaly. The number of the composited events in the model is almost the same as that in the observation over the western Pacific, although it is significantly underestimated over the Indian Ocean. The model successfully represents the westward tilt of the moisture anomaly over the eastern Maritime Continent and the western Pacific, but it is lacking over the western Maritime Continent. The model succeeds in representing the positive moisture anomaly over the convective area but its peak is higher than that in the reanalysis presumably because of the underestimated shallow convective activity. The composited peak free-tropospheric moisture

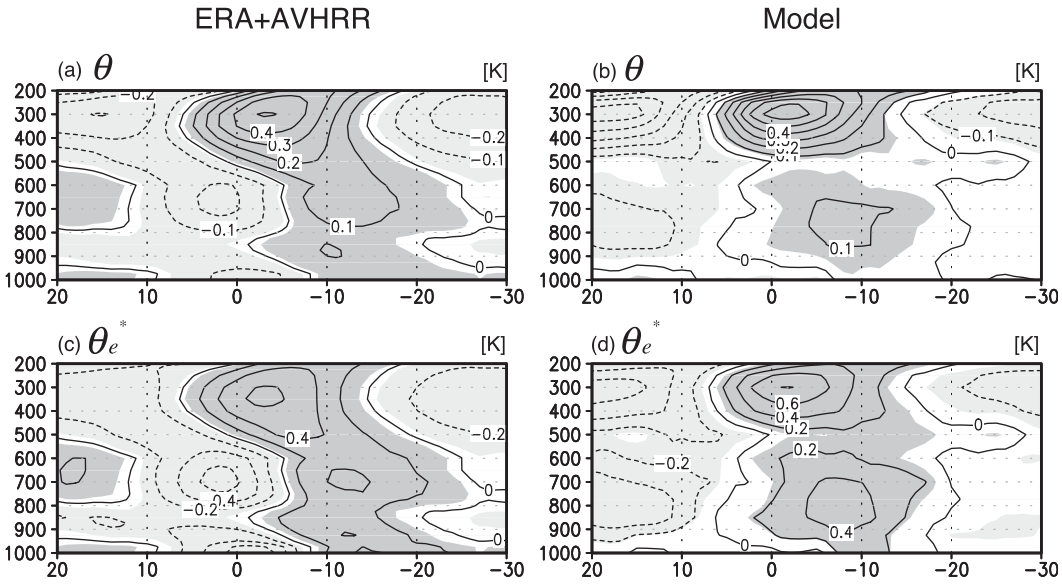

FIG. 14. Latitudinally averaged (a),(b) potential temperature and (c),(d) saturation equivalent potential temperature in (left) ERA-Interim and (right) the model. Ordinate and abscissa are pressure (hPa) and relative time (days), respectively. The 95% significance level is indicated by gray. Units are shown above each panel.

in the model tends to shift more southward than that in the reanalysis, simply because the model MJO-like waves tend to stay over the western Pacific.

The eastward shift of the peak moist static energy for the surface air is well represented in the model, although the shift is slightly smaller than that in the reanalysis, probably corresponding to the less westward tilt of the free-tropospheric humidity. Although the model's surface zonal wind velocity agrees well with the reanalysis, the surface wind speed does not exhibit the westward shift seen in the reanalysis owing to the overestimated magnitude of the surface meridional wind velocity. It leads to the lack of the westward shift in the model's surface latent heat flux.

The positive temperature anomaly in the upper troposphere over the convective area and the more moderate one in the lower to middle troposphere to the east are well captured by the model. However, the model lacks the negative temperature peak in the middle troposphere to the west of the OLR minimum seen in the reanalysis, probably because of the smaller amount of the evaporation by the stratiform precipitation. The model successfully represents the top-heavy profiles of the Q1 and Q2 seen in the reanalysis, although the model exhibits more drying in the lower troposphere, presumably because of the underestimated shallow convective activity. The overall features of the vertical and zonal velocities are well represented by the model. However, the model lacks the westward tilt in Q1, Q2, and the vertical and zonal velocities.

The most outstanding deficiency in the model is the weak convective activity over the Indian Ocean. However, since the climatological precipitation there is greatly improved when coupled with the oceanic model (Watanabe et al. 2010), the behaviors of the model MJO-like waves are expected to be improved by the coupling and additional necessary tuning without changing the model structure.

An outstanding inherent problem in the AGCM seems to be the underestimation of the shallow convective activity over the convective area, which causes the smaller positive anomaly in the lower-tropospheric humidity. While it is common for other GCMs to adopt a shallow convection scheme separately from a deep one in order to enhance the activity, the Chikira–Sugiyama scheme took the approach to represent shallow convection in the same framework as the deep one, but seemingly the scheme does not represent it sufficiently. Additional improvements in this direction are still necessary.

The larger amplitude of the model's upper-tropospheric cloud water than that of the reanalysis presumably causes the overestimated OLR variance. The reason is not clear since many factors are related to it, such as the representation of the detrainment, subgrid PDF, and fallout of precipitation. Although the model does not represent the negative temperature peak in the middle troposphere over 0–5 relative days seen in Fig. 14a, the problem might be solved simply by changing the tuning parameters so as to enlarge the efficiency of the

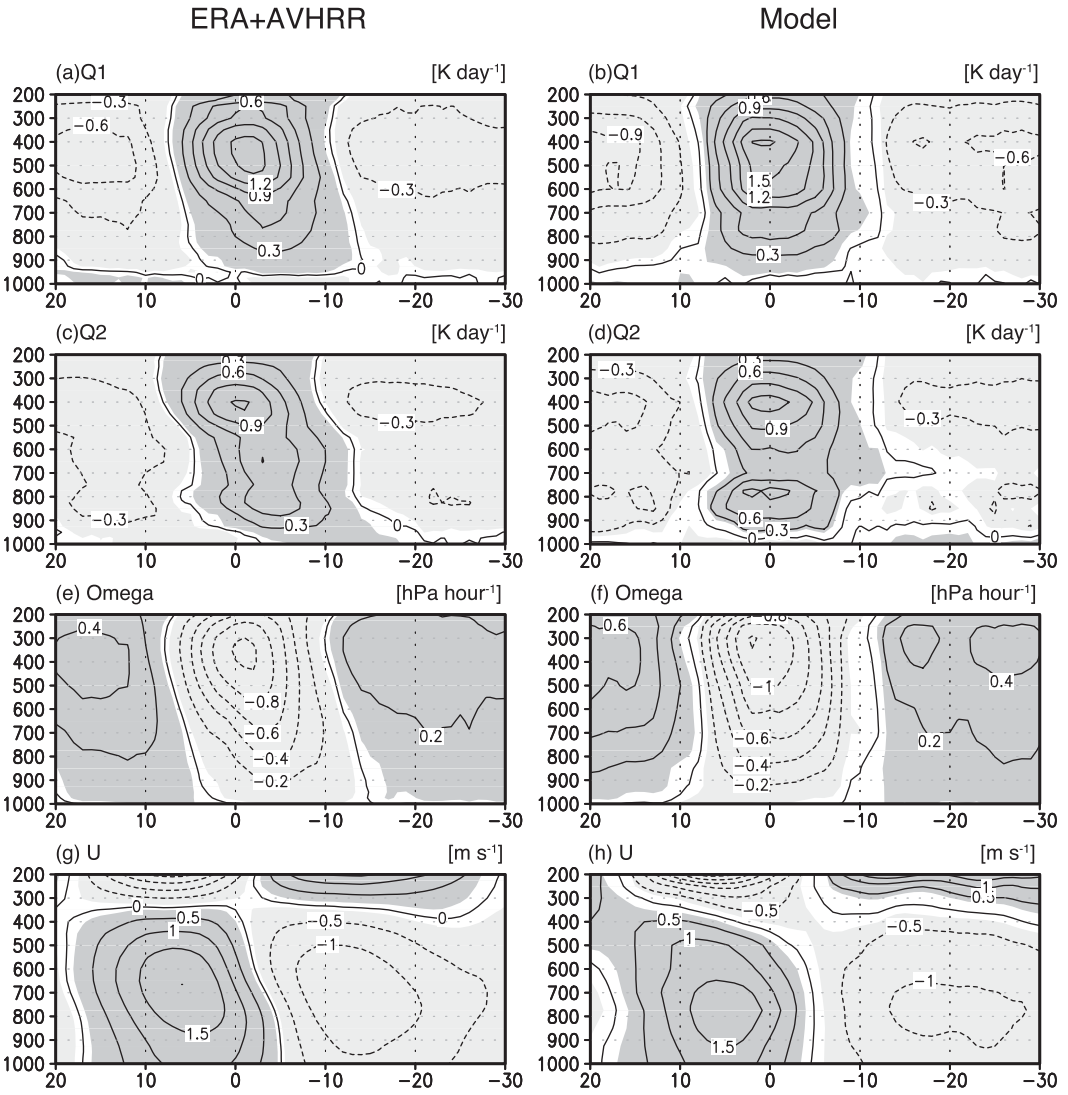

FIG. 15. Latitudinally averaged (a),(b) Q1, (c),(d) Q2, (e),(f) pressure velocity, and (g),(h) zonal velocity in (left) ERA-Interim and (right) the model. Ordinate and abscissa are pressure (hPa) and relative time (days), respectively. The 95% significance level is indicated by gray. Units are shown above each panel.

rainfall evaporation. Such a change may also improve the distribution of the sea surface pressure and thereby surface wind over the convective area.

Despite all the problems described above, the model successfully reproduces the eastward propagation of the convective area and accompanying wind fields to the extent that it can be extracted by the CEOF principal components. The basic features of the composited anomalous fields including moisture, temperature, and vertical and zonal winds resemble those of the ERA-Interim both in the free troposphere and surface air. Hence, the essential dynamics of the MJO is considered to be represented by the model. Part II of this paper builds on this result and further analyzes the variation of the free-tropospheric humidity focusing on the mechanism of the MJO. Thequestion as to why the Chikira–Sugiyama scheme succeeded in representing the MJO to this degree will be discussed through the analysis in Part II.

Acknowledgments. The part of the analysis was made with diagnostic tools developed by the U.S. CLIVAR MJO Working Group. We greatly thank the group, especially Dr. D. Kim, for providing the tool and helpful comments on it. Comments by anonymous reviewers greatly improved this manuscript. The model results were obtained with the Earth Simulator at JAMSTEC. This work was supported by the Innovative

Program of Climate Change Projection for the 21st Century (''Kakushin'' program) from MEXT, Japan.

REFERENCES

Arakawa, A., and W. H. Schubert, 1974: Interaction of a cumulus cloud ensemble with the large-scale environment, Part I. *J. Atmos. Sci.,* **31,** 674–701.

Bechtold, P., M. Köhler, T. Jung, F. Doblas-Reyes, M. Leutbecher, M. J. Rodwell, F. Vitart, and G. Balsamo, 2008: Advances in simulating atmospheric variability with the ECMWF model: From synoptic to decadal time-scales. *Quart. J. Roy. Meteor. Soc.,* **134,** 1337–1351, doi:10.1002/qj.289.

Bergman, J. W., H. H. Hendon, and K. M. Weickmann, 2001: Intraseasonal air–sea interactions at the onset of El Niño. *J. Climate,* **14,** 1702–1719.

Betts, A. K., 1986: A new convective adjustment scheme. Part I: Observational and theoretical basis. *Quart. J. Roy. Meteor. Soc.,* **112,** 677–691.

——, and M. J. Miller, 1986: A new convective adjustment scheme. Part II: Single column tests using GATE wave, BOMEX, ATEX and arctic air-mass data sets. *Quart. J. Roy. Meteor. Soc.,* **112,** 693–709.

Biasutti, M., A. H. Sobel, and Y. Kushnir, 2006: AGCM precipitation biases in the tropical Atlantic. *J. Climate,* **19,** 935–958.

Brown, R. G., and C. Zhang, 1997: Variability of midtropospheric moisture and its effect on cloud-top height distribution during TOGA COARE. *J. Atmos. Sci.,* **54,** 2760–2774.

Chikira, M., 2010: A cumulus parameterization with state-dependent entrainment rate. Part II: Impact on climatology in a general circulation model. *J. Atmos. Sci.,* **67,** 2194–2211.

——, 2013: Eastward-propagating intraseasonal oscillation represented by Chikira–Sugiyama cumulus parameterization. Part II: Understanding moisture variation under weak temperature gradient balance. *J. Atmos. Sci.,* in press.

——, and M. Sugiyama, 2010: A cumulus parameterization with state-dependent entrainment rate. Part I: Description and sensitivity to temperature and humidity profiles. *J. Atmos. Sci.,* **67,** 2171–2193.

CLIVAR Madden–Julian Oscillation Working Group, 2009: MJO simulation diagnostics. *J. Climate,* **22,** 3006–3030.

Del Genio, A. D., and J. Wu, 2010: The role of entrainment in the diurnal cycle of continental convection. *J. Climate,* **23,** 2722–2738.

——, M.-S. Yao, and J. Jonas, 2007: Will moist convection be stronger in a warmer climate? *Geophys. Res. Lett.,* **34,** L16703, doi:10.1029/2007GL030525.

——, Y. Chen, D. Kim, and M.-S. Yao, 2012: The MJO transition from shallow to deep convection in *CloudSat*/CALIPSO data and GISS GCM simulations. *J. Climate,* **25,** 3755–3770.

Deng, L., and X. Wu, 2010: Effects of convective processes on GCM simulations of the Madden–Julian oscillation. *J. Climate,* **23,** 352–377.

Derbyshire, S. H., I. Beau, P. Bechtold, J.-Y. Grandpeix, J.-M. Piriou, J.-L. Redelsperger, and P. M. M. Soares, 2004: Sensitivity of moist convection to environmental humidity. *Quart. J. Roy. Meteor. Soc.,* **130,** 3055–3079.

Donald, A., H. Meinke, B. Power, A. H. N. Maia, M. C. Wheeler, N. White, R. C. Stone, and J. Ribbe, 2006: Near-global impact of the Madden-Julian oscillation on rainfall. *Geophys. Res. Lett.,* **33,** L09704, doi:10.1029/2005GL025155.

Dunkerton, T. J., and M. P. Baldwin, 1995: Observation of 3–6-day meridional wind oscillations over the tropical Pacific, 1973–1992: Horizontal structure and propagation. *J. Atmos. Sci.,* **52,** 1585–1601.

Ferranti, L., T. N. Palmer, F. Molteni, and E. Klinker, 1990: Tropical-extratropical interaction associated with the 30–60 day oscillation and its impact on medium and extended range prediction. *J. Atmos. Sci.,* **47,** 2177–2199.

Fu, X., and B. Wang, 2004: Differences of boreal summer intraseasonal oscillations simulated in an atmosphere–ocean coupled model and an atmosphere-only model. *J. Climate,* **17,** 1263–1271.

Fuchs, Ž., and D. J. Raymond, 2002: Large-scale modes of a nonrotating atmosphere with water vapor and cloud–radiation feedbacks. *J. Atmos. Sci.,* **59,** 1669–1679.

——, and ——, 2005: Large-scale modes in a rotating atmosphere with radiative–convective instability and WISHE. *J. Atmos. Sci.,* **62,** 4084–4094.

Gill, A. E., 1980: Some simple solutions for heat-induced tropical circulation. *Quart. J. Roy. Meteor. Soc.,* **106,** 447–462.

Goswami, B. N., 2005: South Asian monsoon. *Intraseasonal Variability in the Atmosphere-Ocean Climate System,* W. K.-M. Lau and D. E. Waliser, Eds., Praxis, 19–61.

Grabowski, W. W., 2001: Coupling cloud processes with the large-scale dynamics using the Cloud-Resolving Convective Parameterization (CRCP). *J. Atmos. Sci.,* **58,** 978–997.

——, and M. W. Moncrieff, 2004: Moisture–convection feedback in the tropics. *Quart. J. Roy. Meteor. Soc.,* **130,** 3081–3104.

Grant, A. L. M., and A. R. Brown, 1999: A similarity hypothesis for shallow-cumulus transports. *Quart. J. Roy. Meteor. Soc.,* **125,** 1913–1936.

Gregory, D., 2001: Estimation of entrainment rate in simple models of convective clouds. *Quart. J. Roy. Meteor. Soc.,* **127,** 53–72.

Hendon, H. H., 2000: Impact of air–sea coupling on the Madden–Julian oscillation in a general circulation model. *J. Atmos. Sci.,* **57,** 3939–3952.

Hirota, N., Y. N. Takayabu, M. Watanabe, and M. Kimoto, 2011: Precipitation reproducibility over tropical oceans and its relationship to the double ITCZ problem in CMIP3 and MIROC5 climate models. *J. Climate,* **24,** 4859–4873.

Inness, P. M., and J. M. Slingo, 2003: Simulation of the Madden–Julian oscillation in a coupled general circulation model. Part I: Comparison with observations and an atmosphere-only GCM. *J. Climate,* **16,** 345–364.

——, ——, S. J. Woolnough, R. B. Neale, and V. D. Pope, 2001: Organization of tropical convection in a GCM with varying vertical resolution: implications for the simulation of the Madden–Julian oscillation. *Climate Dyn.,* **17,** 777–793.

——, ——, E. Guilyardi, and J. Cole, 2003: Simulation of the Madden–Julian oscillation in a coupled general circulation model. Part II: The role of the basic state. *J. Climate,* **16,** 365–382.

Jia, X., C. Li, J. Ling, and C. Zhang, 2008: Impacts of a GCM's resolution on MJO simulation. *Adv. Atmos. Sci.,* **25,** 139–156.

Kalnay, E., and Coauthors, 1996: The NCEP/NCAR 40-Year Reanalysis Project. *Bull. Amer. Meteor. Soc.,* **77,** 437–471.

Kemball-Cook, S., B. Wang, and X.-H. Fu, 2002: Simulation of the intraseasonal oscillation in the ECHAM-4 model: The impact of coupling with an ocean model. *J. Atmos. Sci.,* **59,** 1433–1453.

Khairoutdinov, M. F., and D. A. Randall, 2001: A cloud-resolving model as a cloud parameterization in the NCAR Community Climate System Model: Preliminary results. *Geophys. Res. Lett.,* **28,** 3617–3620.

Kim, D., and Coauthors, 2009: Application of MJO simulation diagnostics to climate models. *J. Climate,* **22,** 6413–6436.

——, A. H. Sobel, A. D. Del Genio, Y. Chen, S. J. Camargo, M.-S. Yao, M. Kelley, and L. Nazarenko, 2012: The tropical subseasonal variability simulated in the NASA GISS general circulation model. *J. Climate,* **25,** 4641–4659.

Kim, H.-J., K. Takata, B. Wang, M. Watanabe, M. Kimoto, T. Yokohata, and T. Yasunari, 2011: Global monsoon, El Niño, and their interannual linkage simulated by MIROC5 and the CMIP3 CGCMs. *J. Climate,* **24,** 5604–5618.

Krishnamurti, T. N., and D. Subrahmanyam, 1982: The 30–50 day mode at 850 mb during MONEX. *J. Atmos. Sci.,* **39,** 2088–2095.

Lau, W. K.-M., 2005: El Niño Southern Oscillation connection. *Intraseasonal Variability in the Atmosphere-Ocean Climate System,* W. K.-M. Lau and D. E. Waliser, Eds., Praxis, 271–305.

Lee, M.-I., I.-S. Kang, J.-K. Kim, and B. E. Mapes, 2001: Influence of cloud-radiation interaction on simulating tropoical intraseasonal oscillation with an atmospheric general circulation model. *J. Geophys. Res.,* **106** (D13), 14 219–14 233.

——, ——, and B. E. Mapes, 2003: Impacts of cumulus convection parameterization on aqua-planet AGCM simulations of tropical intraseasonal variability. *J. Meteor. Soc. Japan,* **81,** 963–992.

Liebmann, B., and C. A. Smith, 1996: Description of a complete (interpolated) outgoing longwave radiation dataset. *Bull. Amer. Meteor. Soc.,* **77,** 1275–1277.

——, H. H. Hendon, and J. D. Glick, 1994: The relationship between tropical cyclones of the western Pacific and Indian Oceans and the Madden-Julian oscillation. *J. Meteor. Soc. Japan,* **72,** 401–411.

Lin, J.-L., and Coauthors, 2006: Tropical intraseasonal variability in 14 IPCC AR4 climate models. Part I: Convective signals. *J. Climate,* **19,** 2665–2690.

——, M. I. Lee, D. Kim, I. S. Kang, and D. M. W. Frierson, 2008: The impacts of convective parameterization and moisture triggering on AGCM-simulated convectively coupled equatorial waves. *J. Climate,* **21,** 883–909.

Madden, R. A., and P. R. Julian, 2005: Historical perspective. *Intraseasonal Variability in the Atmosphere-Ocean Climate System,* W. K.-M. Lau and D. E. Waliser, Eds., Praxis, 1–18.

Maloney, E. D., 2002: An intraseasonal oscillation composite life cycle in the NCAR CCM3.6 with modified convection. *J. Climate,* **15,** 964–982.

——, 2009: The moist static energy budget of a composite tropical intraseasonal oscillation in a climate model. *J. Climate,* **22,** 711–729.

——, and D. L. Hartmann, 2000: Modulation of hurricane activity in the Gulf of Mexico by the Madden-Julian oscillation. *Science,* **287,** 2002–2004.

——, and ——, 2001: The sensitivity of intraseasonal variability in the NCAR CCM3 to changes in convective parameterization. *J. Climate,* **14,** 2015–2034.

Marshall, A. G., O. Alves, and H. H. Hendon, 2008: An enhanced moisture convergence-evaporation feedback mechanism for MJO air–sea interaction. *J. Atmos. Sci.,* **65,** 970–986.

Matsuno, T., 1966: Quasi-geostrophic motions in the equatorial area. *J. Meteor. Soc. Japan,* **44,** 25–43.

Miura, H., M. Satoh, T. Nasuno, A. T. Noda, and K. Oouchi, 2007: A Madden-Julian oscillation event realistically simulated by a global cloud-resolving model. *Science,* **318,** 1763–1765.

Neelin, J. D., and N. Zeng, 2000: A quasi-equilibrium tropical circulation model—Formulation. *J. Atmos. Sci.,* **57,** 1741–1766.

Neggers, R. A. J., A. P. Siebesma, and H. J. J. Jonker, 2002: A multiparcel method for shallow cumulus convection. *J. Atmos. Sci.,* **59,** 1655–1668.

Numaguti, A., R. Oki, K. Nakamura, K. Tsuboki, N. Misawa, T. Asai, and Y.-M. Kodama, 1995: 4-5-day-period variation and low-level dry air observed in the equatorial western Pacific during the TOGA-COARE IOP. *J. Meteor. Soc. Japan,* **73,** 267–290.

Pan, D.-M., and D. A. Randall, 1998: A cumulus parameterization with a prognostic closure. *Quart. J. Roy. Meteor. Soc.,* **124,** 949–981.

Raymond, D. J., 2001: A new model of the Madden–Julian oscillation. *J. Atmos. Sci.,* **58,** 2807–2819.

——, and Ž. Fuchs, 2009: Moisture modes and the Madden–Julian oscillation. *J. Climate,* **22,** 3031–3046.

Sherwood, S. C., 1999: Convective precursors and predictability in the tropical western Pacific. *Mon. Wea. Rev.,* **127,** 2977–2991.

——, and R. Wahrlich, 1999: Observed evolution of tropical deep convective events and their environment. *Mon. Wea. Rev.,* **127,** 1777–1795.

Slingo, J. M., and Coauthors, 1996: Intraseasonal oscillations in 15 atmospheric general circulation models: Results from an AMIP diagnostic subproject. *Climate Dyn.,* **12,** 325–357.

Sobel, A., and E. Maloney, 2012: An idealized semi-empirical framework for modeling the Madden–Julian oscillation. *J. Atmos. Sci.,* **69,** 1691–1705.

——, and ——, 2013: Moisture modes and the eastward propagation of the MJO. *J. Atmos. Sci.,* **70,** 187–192.

——, J. Nilsson, and L. M. Polvani, 2001: The weak temperature gradient approximation and balanced tropical moisture waves. *J. Atmos. Sci.,* **58,** 3650–3665.

——, S. E. Yuter, C. S. Bretherton, and G. N. Kiladis, 2004: Large-scale meteorology and deep convection during TRMM KWAJEX. *Mon. Wea. Rev.,* **132,** 422–444.

Sperber, K. R., and H. Annamalai, 2008: Coupled model simulations of boreal summer intraseasonal (30–50 day) variability, Part 1: Systematic errors and caution on use of metrics. *Climate Dyn.,* **31,** 345–372.

——, S. Gualdi, S. Legutke, and V. Gayler, 2005: The Madden–Julian oscillation in ECHAM4 coupled and uncoupled general circulation models. *Climate Dyn.,* **25,** 117–140.

——, H. Annamalai, I.-S. Kang, A. Kitoh, A. Moise, A. Turner, B. Wang, and T. Zhou, 2013: The Asian summer monsoon: An intercomparison of CMIP5 vs. CMIP3 simulations of the late 20th century. *Climate Dyn.,* doi:10.1007/S00382-012-1607-6, in press.

Sugiyama, M., 2009: The moisture mode in the quasi-equilibrium tropical circulation model. Part I: Analysis based on the weak temperature gradient approximation. *J. Atmos. Sci.,* **66,** 1507–1523.

Suzuki, T., Y. N. Takayabu, and S. Emori, 2006: Coupling mechanisms between equatorial waves and cumulus convection in an AGCM. *Dyn. Atmos. Oceans,* **42,** 81–106, doi:10.1016/j.dynatmoce.2006.02.004.

Takayabu, Y. N., and T. Nitta, 1993: 3–5 day period disturbances coupled with convection over the tropical Pacific Ocean. *J. Meteor. Soc. Japan,* **71,** 221–246.

——, T. Iguchi, M. Kachi, A. Shibata, and H. Kanzawa, 1999: Abrupt termination of the 1997–98 El Niño in response to a Madden–Julian oscillation. *Nature,* **402,** 279–282.

Tokioka, T., K. Yamazaki, A. Kitoh, and T. Ose, 1988: The equatorial 30–60 day oscillation and the Arakawa-Schubert penetrative cumulus parameterization. *J. Meteor. Soc. Japan,* **66,** 883–901.

Tomita, H., H. Miura, S. Iga, T. Nasuno, and M. Satoh, 2005: A global cloud-resolving simulation: Preliminary results from an aqua planet experiment. *Geophys. Res. Lett.,* **32,** L08805, doi:10.1029/2005GL022459.

Waliser, D. E., K. M. Lau, and J. H. Kim, 1999: The influence of coupled sea surface temperatures on the Madden–Julian oscillation: A model perturbation experiment. *J. Atmos. Sci.,* **56,** 333–358.

——, and Coauthors, 2003: AGCM simulations of intraseasonal variability associated with the Asian summer monsoon. *Climate Dyn.,* **21,** 423–446.

Wang, W., and M. E. Schlesinger, 1999: The dependence on convective parameterization of the tropical intraseasonal oscillation simulated by the UIUC 11-layer atmospheric GCM. *J. Climate,* **12,** 1423–1457.

Watanabe, M., S. Emori, M. Satoh, and H. Miura, 2009: A PDF-based hybrid prognostic cloud scheme for general circulation models. *Climate Dyn.,* **33,** 795–816, doi:10.1007/s00382-008-0489-0.

——, and Coauthors, 2010: Improved climate simulation by MIROC5: Mean states, variability, and climate sensitivity. *J. Climate,* **23,** 6312–6335.

——, M. Chikira, Y. Imada, and M. Kimoto, 2011: Convective control of ENSO simulated in MIROC. *J. Climate,* **24,** 543–562.

Wheeler, M., and G. N. Kiladis, 1999: Convectively coupled equatorial waves: Analysis of clouds and temperature in the wavenumber-frequency domain. *J. Atmos. Sci.,* **56,** 374–399.

——, and H. H. Hendon, 2004: An all-season real-time multivariate MJO index: Development of an index for monitoring and prediction. *Mon. Wea. Rev.,* **132,** 1917–1932.

——, and J. L. McBride, 2005: Australian-Indonesian monsoon. *Intraseasonal Variability in the Atmosphere-Ocean Climate System,* W. K.-M. Lau and D. E. Waliser, Eds., Praxis, 125–173.

Xu, K.-M., 1993: Cumulus ensemble simulation. *The Representation of Cumulus Convection in Numerical Models, Meteor. Monogr.,* No. 46, Amer. Meteor. Soc., 221–235.

Yanai, M., S. Esbensen, and J.-H. Chu, 1973: Determination of bulk properties of tropical cloud clusters from large-scale heat and moisture budgets. *J. Atmos. Sci.,* **30,** 611–627.

Yasunari, T., 1979: Cloudiness fluctuations associated with the Northern Hemisphere summer monsoon. *J. Meteor. Soc. Japan,* **57,** 227–242.

Zhang, G. J., and M. Mu, 2005: Simulation of the Madden–Julian oscillation in the NCAR CCM3 using a revised Zhang–McFarlane convection parameterization scheme. *J. Climate,* **18,** 4046–4064.